doi:10.1038/nature12002

1) Observational data and information flow overview

Figure S 1 shows the principal information flow as well as the observational data used for this study. More information on the different instruments, measurement capabilities, uptime, and retrievals algorithms is available in [1] and references therein. Summit observations used in this study are for the months of July 2010, 2011, and 2012.

Note that the prognostic model used in this study is driven solely by the cloud temperature, T_a, and simulated or observed radiative fluxes. Comparisons between simulated and radiative observed fluxes are shown below in Section 4)c). Comparisons between model-derived 2-m temperatures and observations are shown in Figure 1 (main article) as well as Figure S 10.

Sensitivity studies with the prognostic model were performed by using simulated radiative fluxes and by systematically varying different parameters such as LWP.

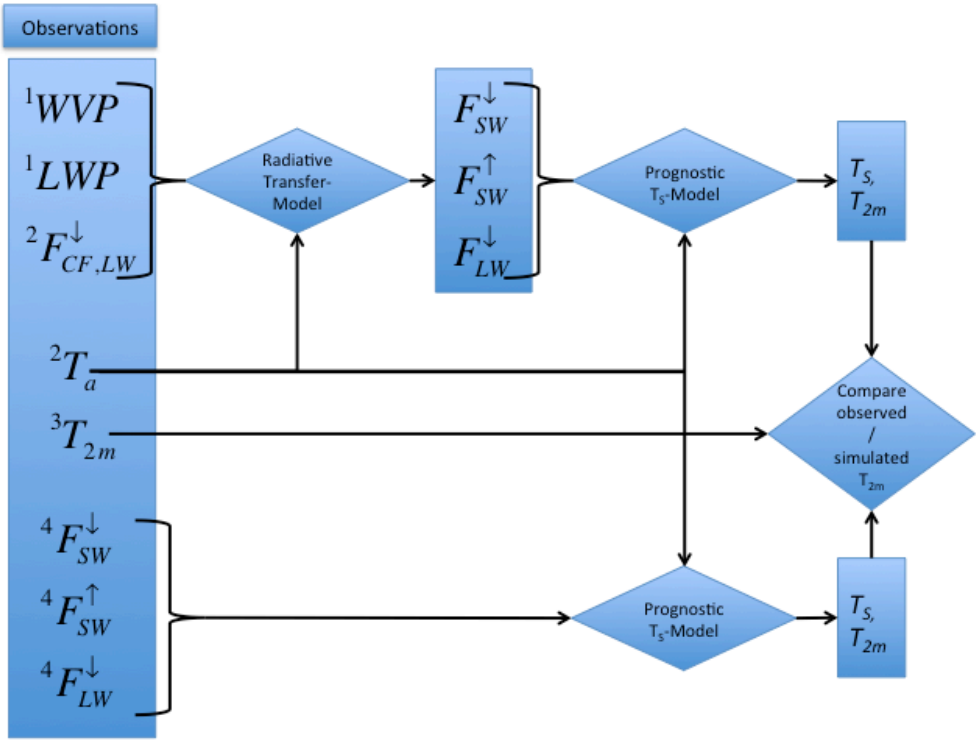

Figure S 1 Overview of data analysis performed in this study. This figure shows the observational data used in the study (left column, titled 'Observations') as well as principal information flow including the radiative transfer model and the prognostic energy balance model (Eq. (1), main article). The left-hand superscripts on the observational data indicate the instruments used, with (1) MWR, (2) Radiosonde, (3) NOAA Met Tower, and (4) broadband radiative flux observations.

2) Detailed description of the prognostic surface energy balance model

a) Parameterization of temperature profile in the surface layer

The temperature profile in the surface layer (SFL) can be approximated by a polynomial profile of the form (Stull [2] and references therein):

$$T(z) = T_a - \left(1 - \frac{z}{H}\right)^{\alpha} \cdot (T_a - T_S) \quad (1)$$

A value of $\alpha = 1$ corresponds to a linear temperature profile, while higher values correspond to a profile with stronger gradients near the surface. Stull[2] suggests values of α between 2 and 3. Different profiles are shown in Figure S 2.

The enthalpy at a given level is given by $h(z) = c_p \cdot T(z)$ and, assuming the density of air to be approximately constant over a shallow layer, the total enthalpy of the SFL per square-meter is:

$$h_{TOT} = \int_0^H \rho \cdot c_p \cdot T(z)\, dz = c_p \rho H \cdot \left[\frac{\alpha}{\alpha+1} T_a + \frac{1}{\alpha+1} T_S\right] \quad (2)$$

For a given shape parameter, this equation can be used to evaluate the change in surface temperature per unit change in enthalpy as:

$$\frac{\partial T_S}{\partial h_{TOT}} = \frac{\alpha+1}{c_p \rho H} \quad (3)$$

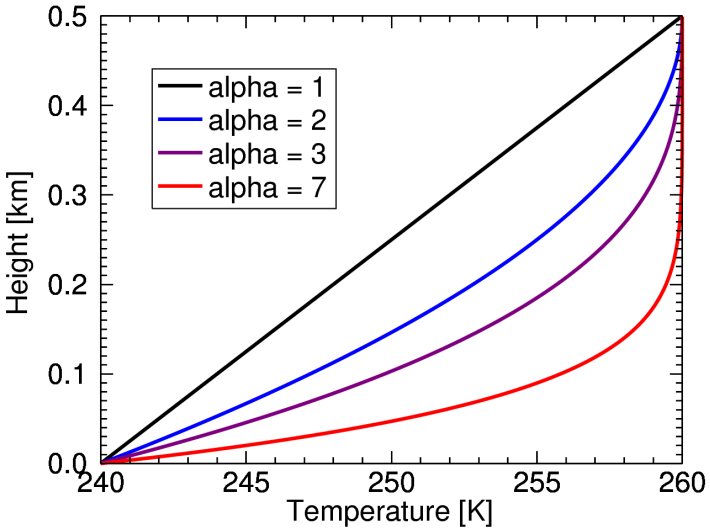

Figure S 2: Example temperature profiles for T_S=240 K, T_a=260 K, H =500 m, and different values of the shape parameter α .

b) Representation of physical processes

Equation (1) allows for the derivation of a simple prognostic equation for the surface temperature assuming the shape of the profile remains constant. The processes captured in Eq. (3) assume that the net radiative flux divergence results in a forcing on the temperature profile in the lower part of the SFL such that the shape parameter remains constant and that the surface temperature responds. The total change in enthalpy due to the radiative flux divergence at the surface is then

$$\frac{\partial h_{TOT}}{\partial t} = \left(F^{\downarrow} - F^{\uparrow} \right), \tag{4}$$

resulting in a temperature change of

$$\frac{\partial T_S}{\partial t} = \frac{\alpha + 1}{c_p \rho H} \left(F^{\downarrow} - F^{\uparrow} \right). \tag{5}$$

This equation allows for an evaluation of the change in surface temperature resulting from net radiative flux divergence. Additional processes acting on the surface temperature are heat fluxes into the ground and atmosphere as well as advection. A simple parameterization of the heat fluxes is one that is proportional to the temperature difference between the top of the SFL and the surface divided by a

relaxation time scale. A simple prognostic model for the surface energy balance can hence be written as:

$$\frac{\partial T_S}{\partial t} = \underbrace{\frac{\alpha+1}{c_p \rho H}\Delta F_{NET}}_{\text{Radiative Forcing}} + \underbrace{\frac{T_i - T_S}{\tau_i}}_{\text{Ice Heat Exchange}} + \underbrace{\frac{T_a - T_S}{\tau_a}}_{\text{Atmospheric Heat Exchange}} \underbrace{-u\frac{\partial T_S}{\partial x}}_{\text{Advection}}, \quad (6)$$

where τ_a, τ_i are relaxation times for the heat exchange processes, u is the surface wind speed and the x-direction is aligned with the surface wind direction. Note, that the advection term is not treated explicitly in the final form of the model for reasons outlined in Section 2)c)iii).

Similar energy balance models have been used before (e.g. [3,4]. The model described here differs in that it describes the temperature profile of the lower atmosphere in a closed form (Equation (1)). Changes in any of the forcings terms can thereby be directly related to resulting surface temperature changes.

c) Parameter choices

i) Atmospheric heat fluxes and relaxation time scale

The order of magnitude of the atmospheric heat relaxation time scale can be evaluated under steady state conditions by setting the left hand side of Equation (6) to zero and neglecting ice heat exchange and advection. It follows that:

$$\tau_a = -\frac{c_p \rho H}{\Delta F_{NET} \cdot (\alpha+1)} \cdot (T_a - T_S) \quad (7)$$

.

A representative set of values for the free parameters for our study are:

$$\begin{aligned} &H = 210\ m,\ \rho = 0.9\ kg/m^3\ ,\alpha = 2,\ T_a = 260\ K, \\ &T_S = 250\ K,\ \ F^{\downarrow} = 250\ W/m^2,\ F^{\uparrow} = \sigma T_S^4 \end{aligned} \quad (8)$$

.

With those values, $\tau_a \approx 8\ hrs$. The obtained relaxation scale values are of the same order of magnitude as the mixing time scales based on SFL-scaling provided in Stull [2] and De Wekker and Whiteman [5]. If different assumptions are made about parameters such as $F^{\downarrow}$, the relaxation time scale would be different. In particular, if $F^{\downarrow}$ was larger, the relaxation time scale would increase as the surface radiative cooling becomes less efficient and hence the downward sensible heat flux counteracting the cooling would also be reduced.

We note here that the relaxation time scale depends on atmospheric stability via $T_a - T_s$, with stability increasing when the surface temperature is colder than the overlying atmosphere (i.e., stronger inversion). In the simple model provided here, a closed functional form of the relaxation time scale is used (see Figure S 3). The sigmoidal functional dependency is chosen to allow for shorter mixing time scales for unstable cases, approaching a typical convective mixing time scale of 0.5 hours, and longer mixing time scales for the most strongly stably stratified surface layers.

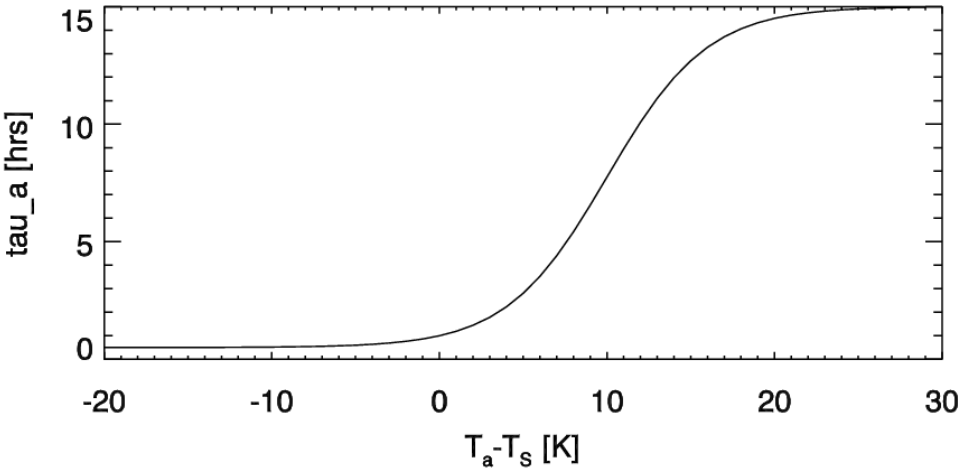

Figure S 3: Parameterization of relaxation time scale τ_a as function of T_a-T_s. The sigmoidal transfer function was chosen to provide reasonable values also for the two limiting cases of an unstable atmosphere with convective mixing (τ_a = 0.5 hrs), and a strongly stably stratified atmosphere with suppressed mixing (τ_a = 15 hrs).

Figure S 4shows the impact of the relaxation time scale parameterization on simulated 2m temperatures for the time period 9-15 July 2012. The yellow curve is identical to the yellow curve in Figure 3 (main article, lower panel) and represents the actual 2m temperature evolution with good accuracy. Figure S 4also shows results for the two limiting cases with constant mixing time scales. If the mixing time scale is kept constant at τ_a=15 hrs (Figure S 4, light blue curve), vertical mixing will remain inefficient even when temperature differences in the SFL are small. This will cause the diurnal cycle to be too strong and the surface to heat too strongly on 11 – 13 July as the energy absorbed at the surface cannot be distributed efficiently in the vertical. For τ_a=0.5 hrs mixing will be too efficient in situations with strong surface-based inversions. This is the case for the surface nighttime cooling on 14 and 15 July, where vertical heat transfer will be too efficient and the surface cannot cool enough (Figure S 4, dark blue curve).

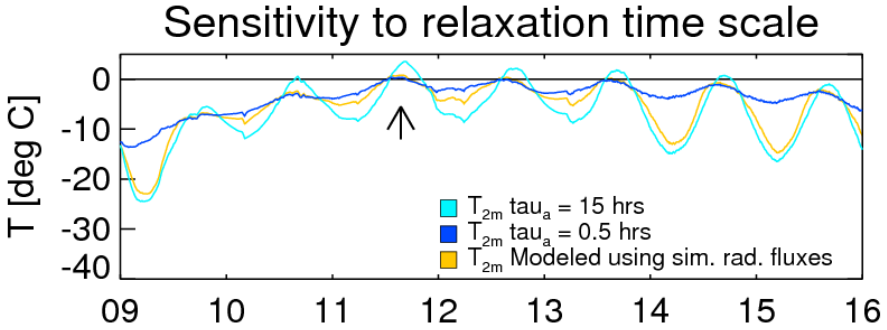

Figure S 4: Sensitivity of simulated surface temperature to the particular choice of the atmospheric relaxation time scale. The yellow curve (same as in main article, Figure 3, lower panel) shows results for the time scale parameterization plotted in Figure S 3 and also used in the main article. The light blue and dark blue curves are results for the two limiting cases of τ_a=15 hrs (slow mixing) and τ_a=0.5 hrs (fast mixing).

ii) Ground heat flux relaxation time scale

The following approximate values for ice density ρ_i and heat capacity $c_{p,i}$ are assumed[3]:

$$\begin{aligned} \rho_i &= 400 \quad \frac{kg}{m^3} \\ c_{p,i} &= 2 \cdot 10^3 \quad \frac{J}{kg \cdot K} \end{aligned} \qquad (9)$$

.

Assuming an ice layer with the above characteristics, a vertical profile of temperature similar to the atmospheric profile with a value of $\alpha_i = 2$ and temperatures T_i at the bottom of the layer and T_s at the top, results in

$$T(z) = T_i - \left(1 - \frac{z}{H_i}\right)^{\alpha_i} \cdot (T_i - T_S) \qquad (10)$$

with z positive downward. The order of magnitude of τ_i can be calculated using an approach similar to the one used for the atmospheric heat exchange (Equation (7)) by specifying values for T_s=233 K and T_i=253 K (i.e., the surface is colder than the deeper snow layer). The relaxation time to maintain this difference under equilibrium can now be calculated assuming a constant T_i and the only process driving T_s lower than T_i to be longwave radiation loss (i.e., a strongly stably stratified wintertime situation). The relaxation time scale can now be derived using the appropriate values for the snow layer as

$$\tau_i = \frac{\rho_i \cdot c_{p,i} \cdot H_i}{(\alpha_i + 1)} \cdot \frac{(T_i - T_S)}{\Delta F_{NET}} \approx 15 hrs \quad (11)$$

.

Assuming that the net heat loss at the surface is roughly 100 W/m^2, this yields a relaxation time of roughly 15 hrs.

iii) Advection

The warm air advection leading to the melting event on 11 July 2012 occurred over two days (9-11 July). From Figure 3 (main paper, upper panel, red temperature curve) one can observe a steady rise in 500m temperature from about -11 deg C at 12 noon on the 9th to about -1 deg C at 12 noon on the 11th, corresponding to an advective change in temperature of 5.0 K/day. A statistical analysis of radiosonde observations in the free atmosphere above the boundary layer (at 500 m) allows for an estimation of the magnitude of the advection term by taking the temporal derivative $\partial T_{500m} / \partial t$. The mean (median) absolute temperature tendency for the three months analyzed is 2.8 (2.0) K/day. Note, that this also includes effects of vertical mixing and a weak diurnal cycle not caused by advection, so that likely the average advective temperature change is slightly smaller.

In comparison, the mean (median) temperature tendency near the surface, $\partial T_{2m} / \partial t$, is 61 (71) K/day, caused by fast temperature changes in response to variations in solar insolation over the course of a day. Advection thus contributes relatively little to the diurnal cycle of surface temperature. (Advection does of course play a critical role at synoptic time scales. In particular, the warming event of 11 July 2012 was triggered by advection of exceptionally warm air as stated above.) For practical purposes, Equation (6) can be simplified by assuming the *surface* advection term to be negligible compared to the other budget terms but by retaining the observed temporal evolution of $T_a(t)$, hence providing $T_a(t)$ as a boundary condition to the model. Implicitly, via downward mixing, changes in $T_a(t)$ caused by advection will then affect surface temperatures as well.

d) Simplifications and assumptions made

For convenience, a number of additional simplifications were introduced to the model. These simplifications will not affect the principal behavior of the model but allow for a more efficient numerical treatment of the problem. In particular:

1. No distinction is made between potential temperature and physical temperature. Note, that the vertical extent of the model is 210 m.
2. The density of the surface layer is assumed to be constant for energetic calculations.
3. The height H of the SFL is assumed to be constant.
4. The latent heat flux is assumed to be small compared to sensible heat exchange.

Assumptions 1 and 2 affect the heat storage in the SFL, i.e. they will affect the value of $c_P \cdot \rho \cdot H$ as well as the actual value of the simulated surface temperature. However, they are of secondary importance compared to the choices made for H and the relaxation time scales. Assumptions 3 and 4 affect the energy balance at the surface under cloud-free conditions and would modify the relaxation time τ_a.

All of these assumptions could be relaxed without changing the model results in principal. However, given the crude treatment of turbulent mixing processes in the model and the analytical temperature profile, a more detailed treatment of these processes will not yield any deeper insights into the temperature response of the SFL to clouds. A more detailed treatment of the issue would have to involve Large Eddy Simulation (LES) studies, which are beyond the scope of this study.

3) Parameterization of radiative fluxes at the surface

Accounting for shortwave and longwave fluxes, the net flux divergence is:

$$\Delta F_{NET} = (F_{LW}^{\downarrow} - F_{LW}^{\uparrow}) + (F_{SW}^{\downarrow} - F_{SW}^{\uparrow}) \quad . \tag{12}$$

The four individual components are modeled as follows. A comparison of observed and simulated radiative fluxes can be found in section 4)c).

a) Longwave fluxes

The upwelling flux at the surface is parameterized as:

$$F^{\uparrow} = \sigma T_S^4 \quad . \tag{13}$$

The downwelling flux under cloudy conditions is modeled as a linear combination of the downwelling clear-sky flux, $F_{CF,LW}^{\downarrow}$, and emission by the cloud, where the cloud is assumed to emit at a temperature T_a, resulting in

$$F^{\downarrow} = t_{C,LW} \cdot F_{CF,LW}^{\downarrow} + \left(1 - t_{C,LW}\right) \cdot \sigma T_a^4 \quad . \tag{14}$$

Cloud-free values of longwave downwelling flux, $F_{CF,LW}^{\downarrow}$, were obtained from ICECAPS [1] radiosonde and station meteorology data using the methodology described in [6]. The effective infrared transmission of the cloud is approximated by:

$$t_{C,IR} = e^{-\delta/\cos(55)} \quad , \tag{15}$$

where the factor 1/cos(55) accounts roughly for the average propagation direction of diffuse radiation under the two-stream assumption. The optical depth in the infrared can be calculated from the relation between liquid water path (LWP), effective radius (r_E), and optical depth (δ_{vis}) in the near-infrared ($LWP = 2/3 \cdot \rho_L \cdot \delta_{VIS} \cdot r_E$). It follows that

$$\delta_{LW} = \frac{1}{2} \cdot \delta_{VIS} = \frac{1}{2} \cdot \frac{LWP}{2/3 \cdot \rho_L \cdot r_E}, \tag{16}$$

where the additional factor of 1/2 roughly accounts for the lower optical depth in the infrared compared to the visible spectral range. Note, that the upwelling flux is also modulated by the surface emissivity, which is set to unity throughout. LWP was obtained from passive microwave observations, and the effective radius r_E was assumed to be 10 µm.

b) Shortwave fluxes

For an incoming solar flux above the cloud, $F_{SOL}^{\downarrow}$, the fraction of solar radiation absorbed by the surface can to first order be derived from a geometrical series expansion including the ice albedo, A_{ICE} , and the shortwave reflectance and transmission of the cloud, $r_{C,SW}$ and $t_{C,SW}$, respectively. The resulting net shortwave flux divergence at the surface will be

$$\left(F_{SW}^{\downarrow} - F_{SW}^{\uparrow}\right) = F_{SOL}^{\downarrow} \cdot \frac{t_{C,SW} \cdot \left(1 - A_{ICE}\right)}{1 - r_{C,SW} A_{ICE}}. \tag{17}$$

Transmittance ($t_{C,SW}$) and reflectance ($r_{C,SW}$) of the cloud were calculated using the 4-band model of Slingo [7]. Note that $F_{SOL}^{\downarrow}$, $t_{C,SW}$, and $r_{C,SW}$ all depend on solar zenith angle. Optical thickness was calculated from LWP using Equation (16) assuming a constant effective radius of 10 µm. Ice albedo was calculated for the four bands by integrating spectrally highly resolved albedo values given in Nolin and Dozier [8] (see also Table S 1).

Table S 1: Ice albedo for the four spectral intervals [7] used to simulate shortwave radiation. Ice albedo values were spectrally averaged from the values reported in Nolin and Dozier [8].

Wavelength Range [µm]	Albedo [1]
0.25 - 0.69	0.98
0.69 - 1.19	0.86
1.19 - 2.38	0.22
2.38 – 4.00	0.04

Visible and near-infrared absorption by water vapor and other gases was calculated using Padé-approximations of broad-band absorption coefficients as outlined in Bennartz and Lohmann [9] and references therein. Water vapor absorption was calculated using microwave radiometer-derived water vapor path, and the ozone column mass was set to 300 DU.

4) Additional information on observations at Summit

a) Cloud fraction statistics at Summit

An overview of the cloud situation at Summit in July 2010, 2011, and 2012 is given in Figure S 5.

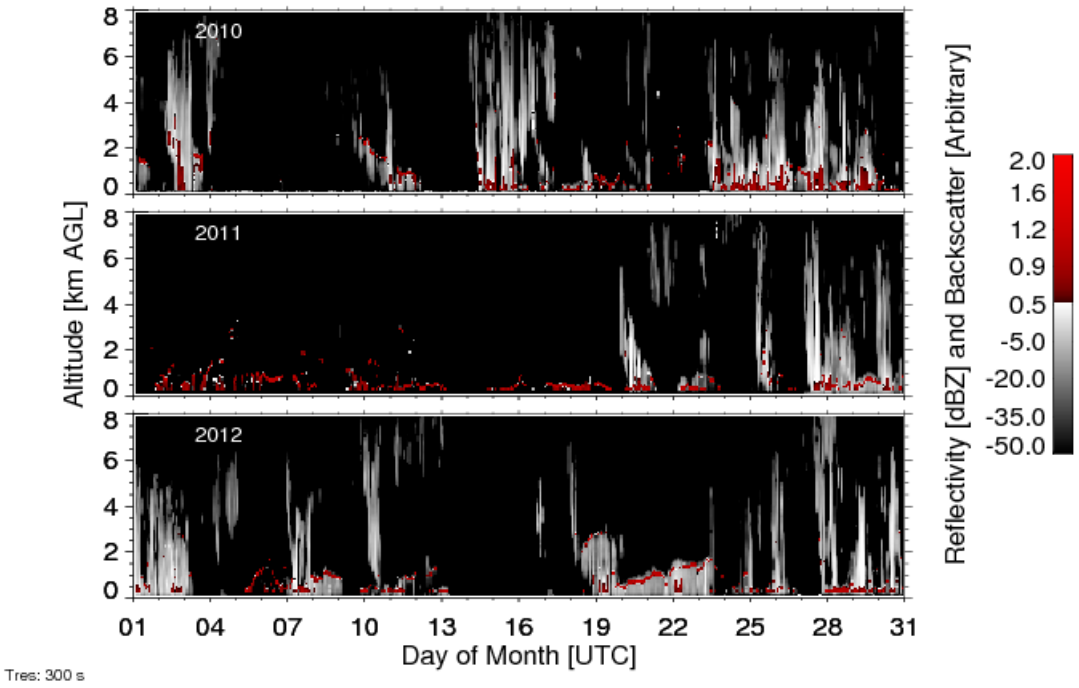

Figure S 5: A composite image of data from the ICECAPS millimeter-wave cloud radar and micropulse lidar at Summit showing the vertical cloud distribution for July 2010, 2011, and 2012. The radar reflectivity data are in gray (dBZ), whereas the backscatter from the lidar are in red. Low liquid water clouds will often attenuate the laser beam, thereby limiting the altitude range that can be sampled by the lidar. The cloud radar was not operational for the first 19 days in July 2011.

Cloud occurrence fractions for these three July months (Table S 2) were calculated from a Vaisala CT25K Ceilometer, which is primarily sensitive to liquid water clouds. The ceilometer also reports cloud base height (CBH) unless there is determined to be obscuration. Cases determined by the ceilometer to be fully obscured (thus do not report a CBH) were considered to be cloudy with a cloud base height near the surface since the obscuration is likely due to low-level fog or heavy precipitation.

Table S 2: Cloud fraction statistics for July 2010, 2011, and 2012 derived from ceilometer observations.

	July 2010	July 2011	July 2012
Total Cloud Fraction [%]	83.1	81.2	75.7
Cloud Fraction [%] Base > 500 m	24.7	22.3	32.1
Cloud Fraction [%] Base < 500 m	58.4	58.9	43.6

b) Liquid water path statistics

Figure S 6illustrates the distribution of microwave radiometer retrieved LWP for the three Julys. The distributions include cases where the ceilometer detects clouds below 500 meters or reported a fully obscured scene. The 5-10 g/m^2 bin has the most frequent occurrence with a decreasing number of observations as the LWP increases. Average values for LWP were 38 ± 38 g/m^2, 34 ± 33 g/m^2, and 39 ± 45 g/m^2 for 2010, 2011, and 2012, respectively, highlighting the high frequency of occurrence of low LWP clouds. Note that the 1-σ uncertainty in the physically-retrieved LWP data is 3-5 g/m^2 because microwave radiance observations at 90 and 150 GHz, which are very sensitive to liquid water [10] are used in addition to the standard 23.8 and 31.4 GHz observations.

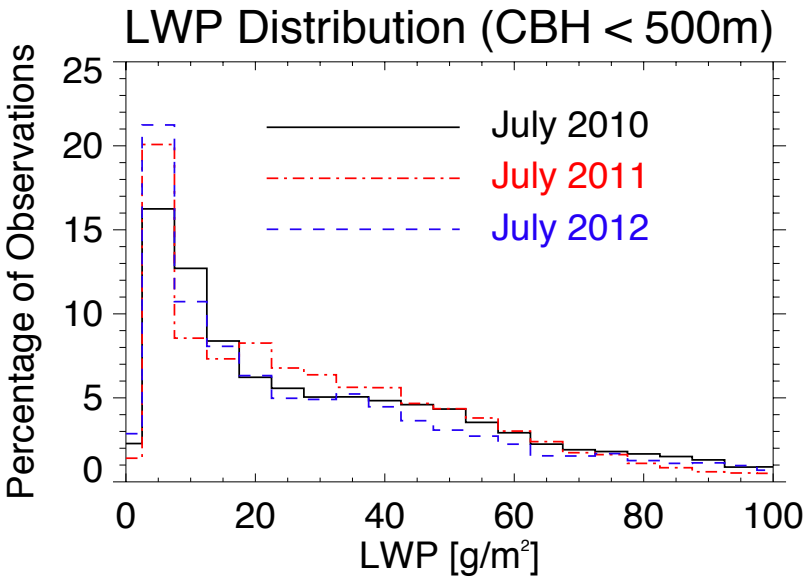

Figure S 6: Histograms of MWR-derived cloud liquid water path for July 2010, 2011, and 2012. Cases with ceilometer-derived CBH higher than 500 m were excluded from this analysis.

c) Comparison of observed and simulated fluxes

Figure S 7– Figure S 9 show comparisons of observed and simulated longwave and shortwave fluxes. While agreement between the observations and simulations is good in general, some discrepancies exist. Notably, the observed and simulated longwave fluxes (Figure S 7) in the cloud-free period 13-16 July 2012 do not agree well. The ultimate reason for this disagreement is unknown. Possible reasons could be LWP retrieval biases, affecting the simulated fluxes, or broadband radiometer calibration issues, affecting the observed fluxes. These deviations between observed and simulated fluxes lead to disagreements in the resulting surface temperature estimates (see main paper, Figure 1, lower panel, differences between the green and yellow curves around 13-16 July 2012).

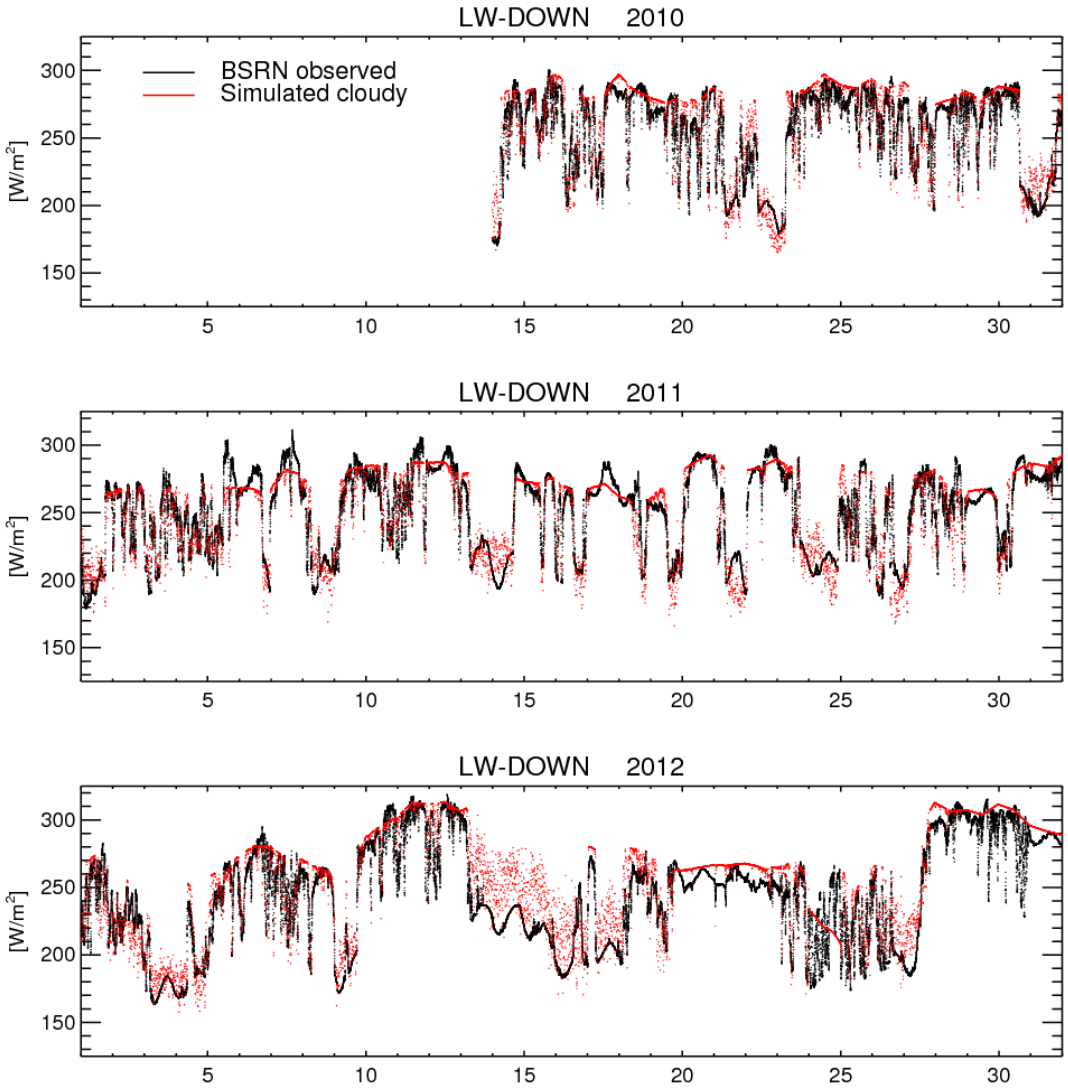

Figure S 7: Comparison of observed and simulated downward longwave fluxes.

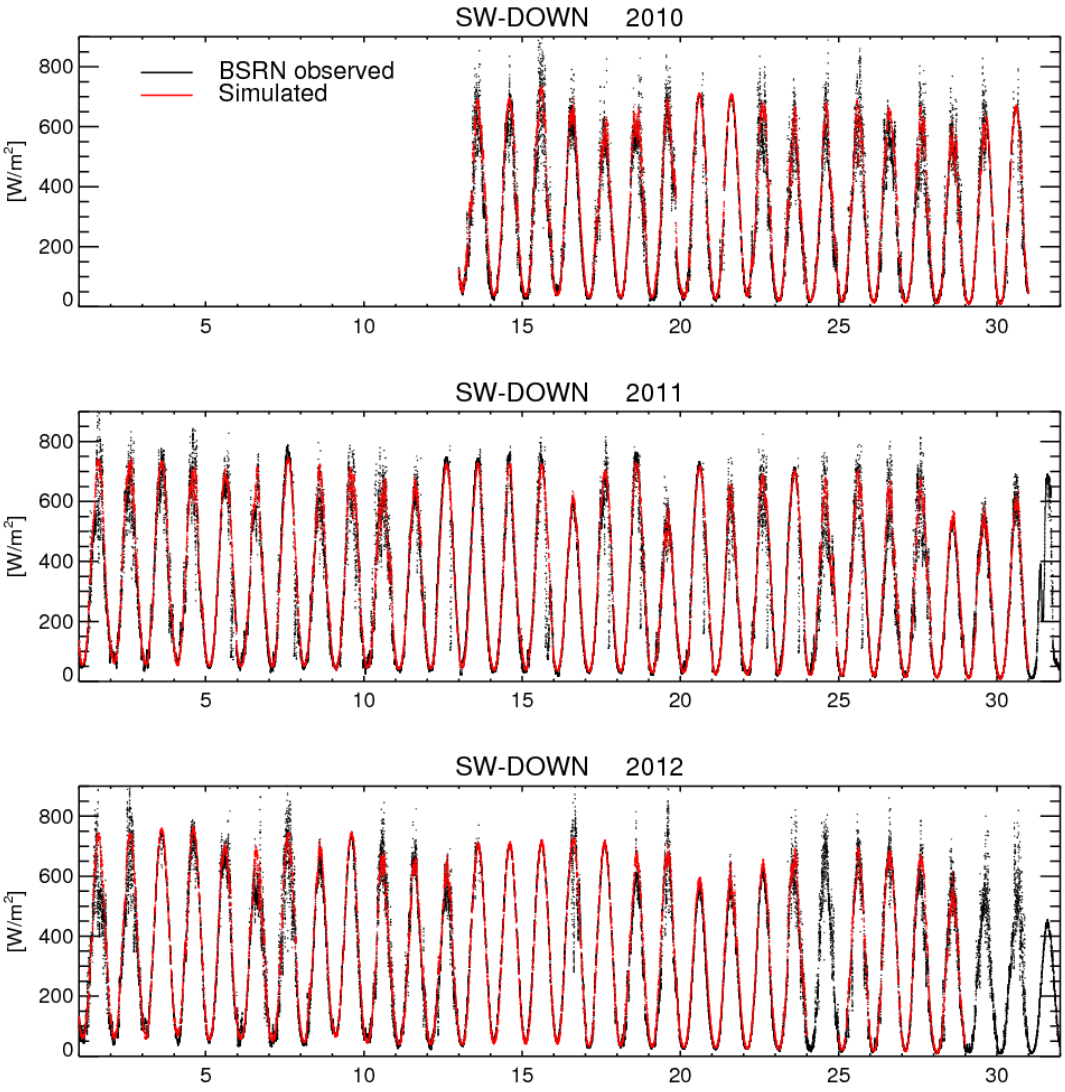

Figure S 8: Comparison observed and simulated downward shortwave fluxes.

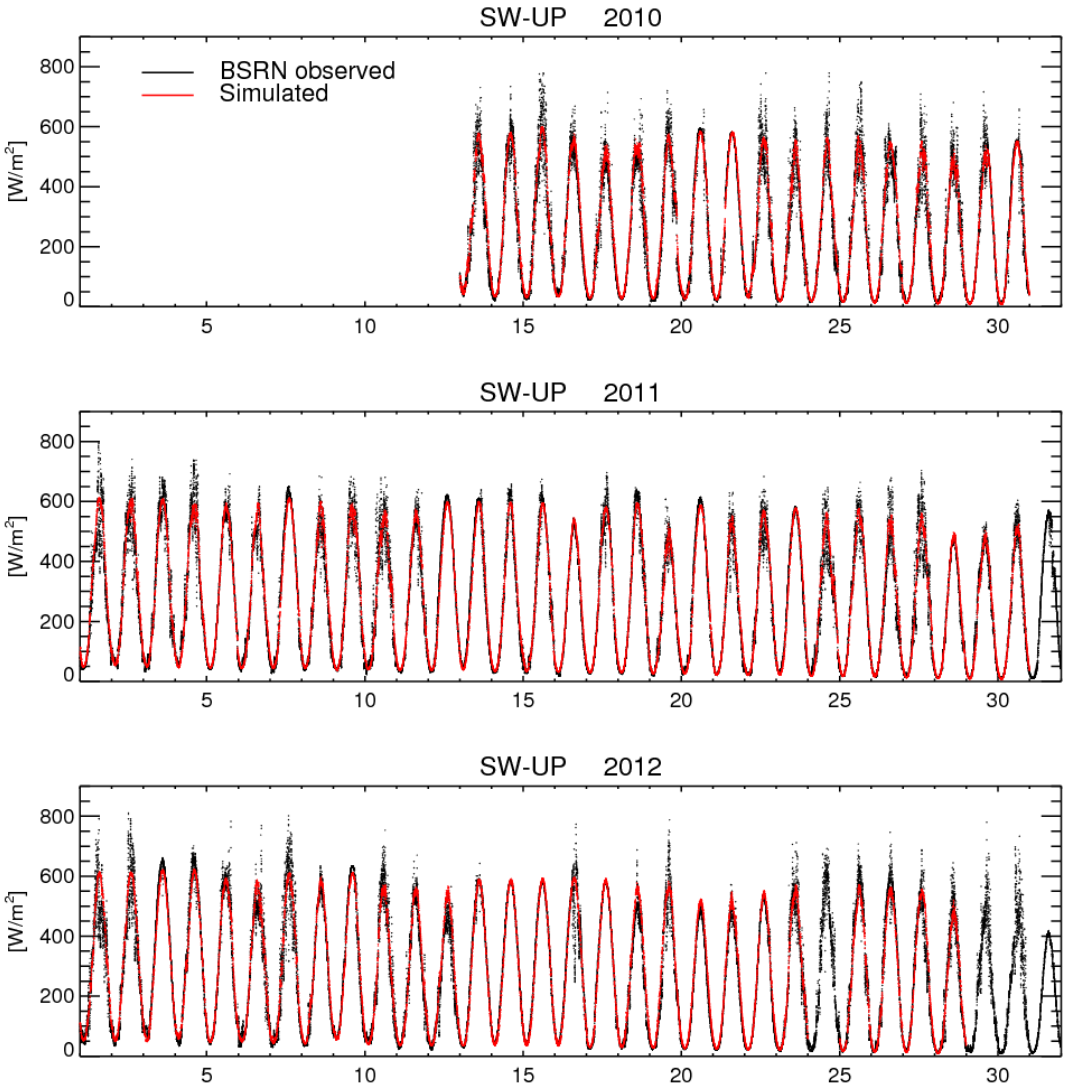

Figure S 9: Observed and simulated upward shortwave fluxes.

5) Comparison of simulated and observed surface temperatures for additional months

In this section we provide modeling results for July 2010 and 2011, similar to those provided in Figure 1 of the main text, to demonstrate the model skill in additional months.

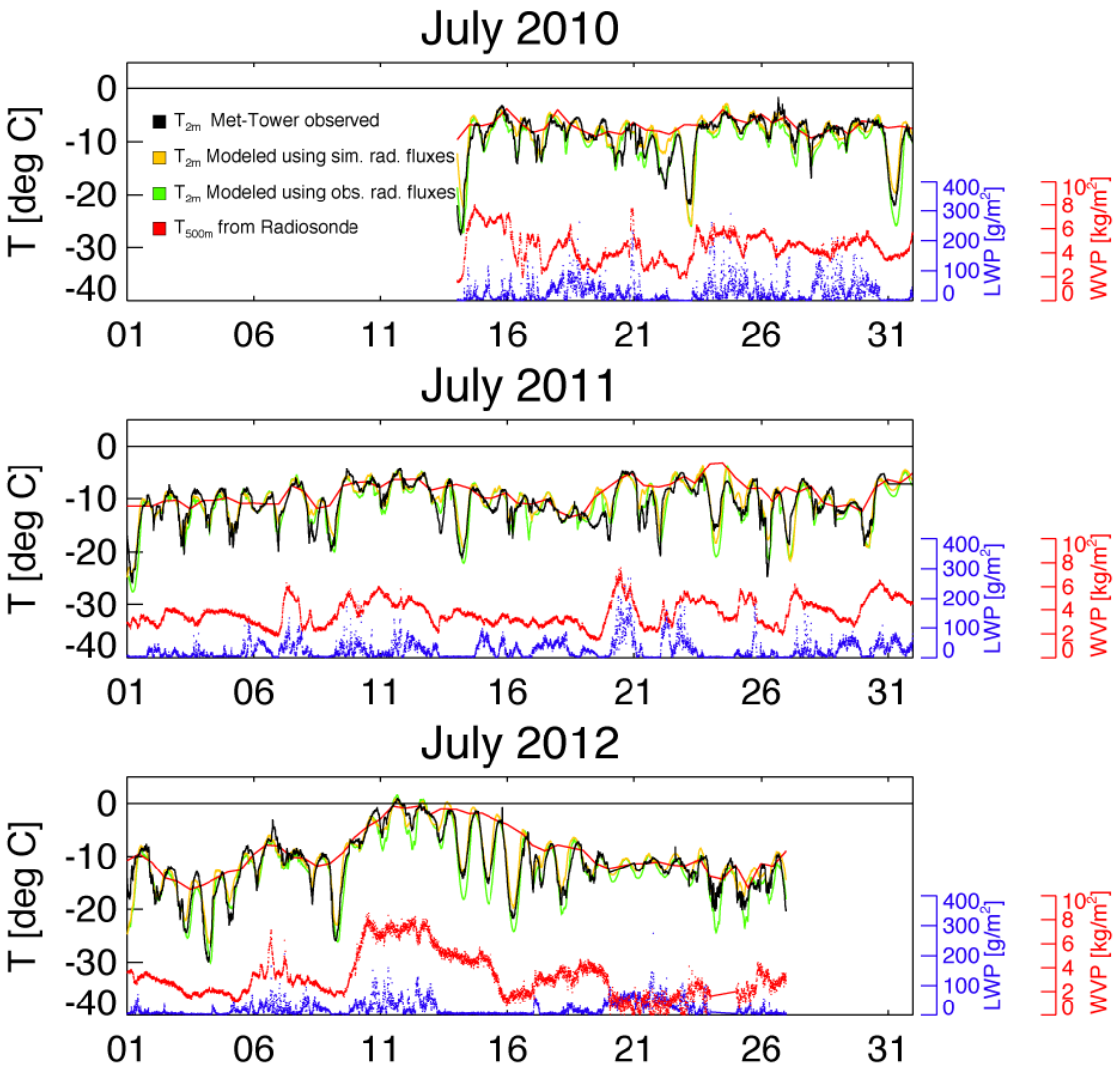

Figure S 10: Temporal evolution of the temperature 2 meters above the surface for July 2010, 2011, 2012. The black curve shows the surface 2-m temperature observed by the NOAA meteorological tower. The red curve shows the temperatures observed by radiosonde at 500 above ground. The green curve shows the temperature development simulated using the surface energy balance model driven by observed radiative fluxes (see also Figure 1, main article). The yellow curve shows the temperature development simulated using the surface energy balance model driven by simulated radiative fluxes based on water vapor path (WVP) and liquid water path (LWP). The blue (red) dots with separate axes show the corresponding LWP (WVP) values observed by an upward looking microwave radiometer.

6) Information on additional observational sites

The liquid water path statistics in Figure 3 (main article) rely on Microwave Radiometer observations taken during four long-term ground-based Arctic experiments. Information about the datasets used is given in Table S 3 below. The ERA-Interim histograms shown in Figure 3 a-d (main article) were also restricted to only cover time periods where observational data was available as well.

Table S 3: Summary of sample time frame, data source, and retrieval method for microwave radiometer (MWR) derived liquid water path values used in Figure 3 (main article). MWRRET is a physical retrieval derived by *Turner et al.*[11] using two frequencies at the Barrow and Eureka sites and four frequencies at Summit [1]. The SHEBA data is derived from a statistical technique based on climatological Barrow soundings, the cloud liquid dielectric model of Liebe[12], and the clear-air absorption model of Rosenkranz[13]. The Barrow data is available from the Atmospheric Radiation Measurement Archive[14]. The Eureka, SHEBA, and Summit data sets are available at the NOAA Earth Systems Research Laboratory public ftp server[15]. Most of the data is continuous, however there is a brief gap in the Summit data during repair to the microwave radiometer scene mirror.

Arctic Site	Retrieval Type	Data Source	Time Range
Barrow, Alaska	MWRRET, Physical 23.8GHz, 31.4GHz	ARM Archive	April 1, 2001 – March 23, 2011
Eureka, Canada	MWRRET, Physical 23.8GHz, 31.4GHz	NOAA, ESRL	August 6, 2008 – June 30, 2010
SHEBA, Arctic Ocean	Liljegren, Statistical 23.8GHz, 31.4GHz	NOAA, ESRL	December 6, 1997 – September 9, 1998
Summit, Greenland	MWRRET, Physical 23.8GHz, 31.4GHz, 90.0GHz, 150.0GHz	NOAA, ESRL	July 14 – October 4, 2010, December 30, 2010 – July 31, 2012

7) Acronyms and Symbols

a) Acronyms

ARM	Atmospheric Radiation Measurement
CBH	Cloud Base Height
DOE	Department of Energy
ECMWF	European Centre for Medium-Range Weather Forecasting
ESRL	NOAA Earth System Research Laboratory
GIS	Greenland Ice Sheet
ICECAPS	Integrated Characterization of Energy, Clouds, Atmospheric state, and Precipitation at Summit
LWP	Liquid Water Path
MODIS	Moderate Resolution Imaging Spectroradiometer
MWR	Microwave Radiometer
PAERI	Polar Atmospheric Emitted Radiance Interferometer
SHEBA	Surface Heat Budget of the Arctic Ocean Project
SFL	Surface Layer
WVP	Water Vapor Path

b) Symbols

$\alpha_{(a\|i)}$	:	Profile shape parameter (atmosphere or ice)
T_a	:	Cloud temperature
T_S	:	Surface temperature
H	:	Height of SFL
τ_a	:	Atmospheric heat exchange relaxation time scale
τ_i	:	Ground heat exchange relaxation time scale
ε_S	:	Surface emissivity
t	:	Time
$\delta_{(SW\|LW)}$	:	Cloud optial depth (SW or LW)
$F^{\downarrow}_{(SW\|LW)}$	:	Radiative flux surface, downward (SW or LW)
$F^{\uparrow}_{CF,LW}$	:	Longwave flux surface, downward, cloud-free
$F^{\uparrow}_{(SW\|LW)}$	:	Radiative flux surface, upward (SW or LW)
r_E	:	Cloud effective radius
ρ_L	:	Density of liquid water
h	:	Enthalpy
h_{TOT}	:	Total enthalpy in SFL per m^2
c_p	:	Specific heat capacity of dry air
$T_{S,SS}$	:	Surface temperature at steady state
u	:	Wind speed
$t_{C,(SW\|LW)}$	:	Transmission of cloud SW or LW
$r_{C,SW}$	:	Shortwave cloud reflectance
A_{ICE}	:	Ice Albedo

8) Additional References

1 Shupe, M. D. *et al.* High and Dry: New Observations of Tropospheric and Cloud Properties above the Greenland Ice Sheet. *B Am Meteorol Soc* **In press** (2012).

2 Stull, R. B. *Introduction to Boundary Layer Meteorology*. (Kluwer academic Press, 1988).

3 Bintanja, R. & van den Broeke, M. THE INFLUENCE OF CLOUDS ON THE RADIATION BUDGET OF ICE AND SNOW SURFACES IN ANTARTICA AND GREENLAND IN SUMMER. *International Journal of Climatology* **16**, 1281-1296 (1996).

4 Ohmura, A. Physical basis for the temperature-based melt-index method. *J Appl Meteorol* **40**, 753-761, doi:10.1175/1520-0450(2001)040<0753:pbfttb>2.0.co;2 (2001).

5 De Wekker, S. F. J. & Whiteman, C. D. On the time scale of nocturnal boundary layer cooling in valleys and basins and over plains. *J Appl Meteorol Clim* **45**, 813-820, doi:10.1175/jam2378.1 (2006).

6 Cox, C. J., Walden, V. P. & Rowe, P. M. A comparison of the atmospheric conditions at Eureka, Canada, and Barrow, Alaska (2006–2008). *Journal of Geophysical Research* **117**, doi:10.1029/2011jd017164 (2012).

7 Slingo, A. A GCM Parameterization for the Shortwave Radiative Properties of Water Clouds. *Journal of the Atmospheric Sciences* **46**, 1419-1427 (1989).

8 Nolin, A. W. & Dozier, J. A Hyperspectral Method for Remotely Sensing the Grain Size of Snow. *Remote Sens Environ* **74**, 207-216 (2000).

9 Bennartz, R. & Lohmann, U. Impact of improved near infrared water vapor line data on absorption of solar radiation in GCMs. *Geophys Res Lett* **28**, 4591-4594 (2001).

10 Crewell, S. & Lohnert, U. Accuracy of cloud liquid water path from ground-based microwave radiometry - 2. Sensor accuracy and synergy. *Radio Sci* **38**, doi:10.1029/2002rs002634 (2003).

11 Turner, D. D. *et al.* Retrieving liquid water path and precipitable water vapor from the atmospheric radiation measurement (ARM) microwave radiometers. *Ieee T Geosci Remote* **45**, 3680-3690, doi:10.1109/tgrs.2007.903703 (2007).

12 Liebe, H. J., Hufford, G. A. & Manabe, T. A Model for the Complex Permittivity of Water at Frequencies Below 1 Thz. *Int J Infrared Milli* **12**, 659-675 (1991).

13 Rosenkranz, P. W. Water vapor microwave continuum absorption: A comparison of measurements and models (vol 33, pg 919, 1998). *Radio Science* **34**, 1025-1025 (1999).

14 http://www.archive.arm.gov/

15 ftp://ftp1.esrl.noaa.gov/psd3/arctic/